Temperature control on CO_2 emissions from the weathering of sedimentary rocks

Guillaume Soulet[1*†], Robert G. Hilton[1*], Mark H. Garnett[2], Tobias Roylands[1], Sébastien Klotz[3], Thomas Croissant[1], Mathieu Dellinger[1], Caroline Le Bouteiller[3]

[1]Department of Geography, Durham University, South Road, Durham DH1 3LE, United Kingdom

[2]NEIF Radiocarbon Laboratory, Rankine Avenue, East Kilbride, Glasgow G75 0QF, UK

[3]Univ. Grenoble Alpes, INRAE, UR ETNA, 2 rue de la papeterie, BP 76, 38402 Saint-Martin-d'Hères, Cedex, France

†Present address: Ifremer, GM, F-29280 Plouzané, France

Correspondence to: G Soulet (guillaume.soulet@ifremer.fr) and RG Hilton (r.g.hilton@durham.ac.uk)

Abstract

Sedimentary rocks can release carbon dioxide (CO_2) during the weathering of rock organic carbon and sulfide minerals. This sedimentary carbon could act as a feedback on Earth's climate over millennial to geological timescales, yet the environmental controls on the CO_2 release from rocks are poorly constrained. Here, we directly measure CO_2 flux from weathering of sedimentary rocks over 2.5 years at the Draix-Bléone Critical Zone Observatory, France. Total CO_2 fluxes approached values reported for soil respiration, with radiocarbon analysis confirming the CO_2 source from rock organic carbon and carbonate. The measured CO_2 fluxes varied seasonally, with summer fluxes five times larger than winter fluxes, and were positively correlated with temperature. The CO_2 release from rock organic carbon oxidation increased by a factor of 2.2 when temperature increased by 10°C. This temperature sensitivity is similar to that of degradation of recent-plant-derived organic matter in soils. Our flux measurements identify sedimentary rock weathering as a positive feedback to warming, which may have operated throughout Earth's history to force the surface carbon cycle.

Main text

Sedimentary rocks contain vast stores of carbon in the form of organic carbon (rock-derived OC, or OC_{petro}) and carbonate minerals (for example calcite; $CaCO_3$), equating to 130,000 times that of the pre-industrial atmosphere[1]. When exhumation and erosion expose sedimentary rocks to the atmosphere and hydrosphere[2,3], oxidative weathering processes can release CO_2 through three main pathways. The oxidation of OC_{petro} by atmospheric dioxygen (O_2) (ref. [4,5]) leads to CO_2 emissions to the atmosphere:

$$CH_2O + O_2 \rightarrow CO_{2,(g)} + H_2O \qquad \text{(R1)}$$

The second pathway is via the oxidation of sulfide minerals (FeS_2; e.g. pyrite) which produces sulfuric acid (H_2SO_4). This can dissolve carbonate minerals and release CO_2 immediately to the atmosphere (ref. [6–8]):

$$4FeS_2 + 15O_2 + 14H_2O \rightarrow 4Fe(OH)_3 + 8H_2SO_4 \qquad \text{(R2)}$$

$$CaCO_3 + H_2SO_4 \rightarrow CO_{2,(g)} + H_2O + Ca^{2+} + SO_4^{2-} \qquad \text{(R3)}$$

Alternatively, the carbon can enter the bicarbonate pool of rivers and be transferred to the ocean. The CO_2 release to the atmosphere is then delayed by an order of 10^4 years, i.e., the timescale of the carbonate precipitation in the ocean[6,9]:

$$2CaCO_3 + H_2SO_4 \rightarrow 2Ca^{2+} + 2HCO_3^- + SO_4^{2-} \qquad \text{(R4)}$$

$$Ca^{2+} + 2HCO_3^- \rightarrow CaCO_3 + CO_{2,(g)} + H_2O \qquad \text{(R5)}$$

A third pathway of CO_2 release from rock can occur following the weathering of carbonate by carbonic acid (H_2CO_3), produced by the dissolution of atmospheric CO_2 in meteoritic water[6], followed by the addition of sulfuric acid to that dissolved inorganic carbon pool:

$$H_2O + CO_{2,(atm)} \rightarrow H_2CO_3 \quad \text{(R6)}$$

$$CaCO_3 + H_2CO_3 \rightarrow Ca^{2+} + 2HCO_3^- \quad \text{(R7)}$$

$$Ca^{2+} + 2HCO_3^- + H_2SO_4 \rightarrow 2CO_{2,(g)} + 2H_2O + Ca^{2+} + SO_4^{2-} \quad \text{(R8)},$$

where one mole of the resultant CO_2 release derives from carbonate.

The global fluxes of CO_2 from sedimentary rock weathering are key players in the geological carbon cycle[3]. Sedimentary rocks dominate Earth's near surface, covering ~64% of the continental area[10] and store an estimated 1.1 x 10^6 megatonnes (10^{12} grams, MtC) of OC_{petro} in the upper 1 m alone[11]. Chemical weathering is estimated to release 40 – 100 MtC.y^{-1} by OC_{petro} oxidation (ref. [12]). The co-occurrence of sulfide and carbonate minerals is less well known, as are the global weathering fluxes, but ~31-36 MtC.y^{-1} is estimated to be released from sulfide oxidation coupled to carbonate dissolution[9,13]. These CO_2 emissions are similar to the 79 ± 9 MtC.y^{-1} released by volcanism[14].

While the global fluxes are known to be important, the sensitivity of CO_2 emissions from sedimentary rock weathering to climate (temperature and hydrology) remains unconstrained. OC_{petro}, in particular, has been previously viewed as relatively unreactive in the weathering zone[15]. Most of our insight on the patterns and controls on CO_2 emissions from oxidative weathering come from studies of geochemical tracers dissolved in river waters[6,7,16–18]. These studies have highlighted the important role of erosion, which supplies OC_{petro} and sulfides to the near-surface zone of oxidative weathering, for setting the rates of CO_2 release[7,17,19]. However, these indirect estimates average over catchment areas that integrate reactions operating under variable hydrologic and temperature conditions. For instance, recent work has highlighted that historical increases in sulfate fluxes in alpine rivers could reflect sulfide oxidation responding to warming, but direct evidence was lacking[20]. To move forward, we use a newly designed method which allows the release of CO_2 during sedimentary rock

weathering to be measured directly at the scale of the outcrop[21]. We directly measure, for the first time, monthly to annual variability in CO_2 fluxes from oxidative weathering of rocks, allowing us to constrain how they are moderated by changing temperature.

New measurements of rock weathering and CO_2 release

We installed five rock chambers (Fig. 1, Methods) in December 2016 in the Laval catchment (0.86 km^2) of the INRAE Draix-Bléone observatory, France, an OZCAR Critical Zone Observatory[22,23] with four decades of measurements of physical (e.g., river solid load), chemical (e.g., river dissolved chemistry) and meteorological (e.g., air temperature, rainfall, river discharge) parameters[22,24,25]. The catchment is composed of Jurassic marls that have features that are likely to be widespread in shales and other sedimentary rocks: they are bedded on the centimetre scale[26] and fractured at the decimetre-to-meter scale[27]; and they contain OC_{petro} concentrations of ~0.5 w% (ref. [25] and Supplementary Table 1), which is lower than a global compilation of Phanerozoic shales, with OC_{petro} ~1 to 3 w% (ref. [28]); and they have undergone moderate thermal maturation at temperatures not exceeding 410°C (ref. [29]). The marls also contain sulfide minerals[29] (~0.6 w% sulfur; Supplementary Table 1), and high concentrations of carbonate minerals (~45 w%; Supplementary Table 1). In this catchment, bare rock outcrops over 68% of the catchment surface area and a combination of steep slopes, frost-shattering in winter months, intense rainfall during storms and finely bedded rocks lead to high erosion rates of 7 to 10 $mm.year^{-1}$ (ref. [21,22,25]) which are characteristic of many steep, sedimentary-rock dominated catchments[3]. Previous work[24] has established that the Laval stream has a low bicarbonate to sulfate ion ratio of ~0.35, indicating widespread sulfide oxidation, and suggesting CO_2 emissions through carbonate weathering via reactions (R3) and (R7-8).

To establish the environmental controls on sedimentary rock weathering, we measured CO_2 emissions in rock chambers (Methods) on seasonal visits for 2.5 years from December

2016 to May 2019. The CO_2 was sampled using zeolite molecular sieves, following an active CO_2 trapping method[21] (Methods). The stable carbon isotopes ($\delta^{13}C$) and radiocarbon activity ($F^{14}C$) of CO_2 were measured to fingerprint its source[21]. The $F^{14}C$ of CO_2 was generally low, confirming a geological source (OC_{petro} and carbonates) from the weathering of marls (Reactions. R1, R3 and R7, Fig. 2). The chambers were installed on bedrock outcrops devoid of recent soil organic matter and with no evidence for root penetration (Fig. 1a). The presence of ^{14}C in the CO_2 samples can result from the input of atmospheric CO_2 to a dissolved inorganic carbon pool via the carbonic acid weathering of carbonate (Reaction R7-8), and/or minor leaks from the atmosphere during sampling (Methods).

The measured total CO_2 fluxes derived from pyrite oxidation combined to carbonate dissolution pathways (Reactions R3 and R7-8) plus OC_{petro} oxidation (Reaction R1) in the Laval catchment approach those of soil respiration[30] (Extended Data Fig. 1). We note caution in upscaling these values, as the volume of rock porosity that has been captured could vary between chambers. The total CO_2 fluxes displayed temporal and spatial variability (Fig. 3a): at chamber H6, fluxes varied between 270 $mgC.m^{-2}.day^{-1}$ in December 2016, to 3040 $mgC.m^{-2}.day^{-1}$ in October 2017 (Fig. 3a). Changes in the CO_2 flux showed a marked seasonal pattern, with warm months characterized by higher CO_2 fluxes (Fig. 3a). CO_2 emissions measured at chamber H4 – located one metre below chamber H6 – were always lower than H6 (Fig. 3a).

Temperature and hydrological controls on CO_2 release

We found a common temperature response to the rock-derived CO_2 emissions across our chambers. For each chamber, the measured total CO_2 flux was positively correlated to the daily-averaged temperature measured in the chamber (Methods) through a growth exponential model (Fig. 4a and Supplementary Table 2):

$$F = F_0 \times \exp(\alpha T) \quad (1),$$

where, F is the CO_2 flux (in $mgC.m^{-2}.d^{-1}$), T is the temperature in the chamber (in °C), F_0 is the amplitude (or the CO_2 flux at 0°C), α is the growth rate parameter (in $°C^{-1}$). The growth rate parameter α is similar for each chamber, with values ranging from 0.057 to 0.079 $°C^{-1}$ (Supplementary Table 2). When we normalise the measured CO_2 flux to the amplitude parameter (F/F_0), the five chambers reveal a coherent seasonal pattern in the CO_2 flux: on average, summer fluxes (June-July-August) are five times larger than winter fluxes (December-January-February) (Fig. 4b). Using the normalized flux data from five chambers over 2.5 years, the growth rate parameter α is 0.070 ± 0.007 $°C^{-1}$ (Fig. 4b and Supplementary Table 2).

The absolute total CO_2 fluxes (Fig. 3a-4a) and the amplitude parameter (F_0) vary between chambers despite their close proximity (Fig. 1, Methods), with F_0 between 35 and 626 $mgC.m^{-2}.d^{-1}$ (Supplementary Table 2). The F_0 value is positively correlated with the elevation of the chamber above the Laval river bed ($r^2 = 0.98$; n = 5; Fig. 5), suggesting the absolute total fluxes relate to the relative position of the chamber above the water table. At higher elevations, diffusion of gaseous O_2 into the rock may promote oxidation of pyrite and OC_{petro} and gaseous CO_2 can diffuse out of the rock face. Closer to the water table, water-filled pores may slow down diffusion of gaseous O_2 and CO_2, reducing the OC_{petro} oxidation and carbonate dissolution by sulfuric acid (Reactions R1 and R3), while also exporting some carbon as dissolved inorganic carbon to the river[31,32]. However, as carbonic acid is supplied by infiltrating water, carbonate dissolution by the carbonic acid pathway (Reaction R7) may be predominant closer to the water table, although still limited by the presence of sulfuric acid to degas CO_2 (Reaction R8). O_2 diffusion in gas/water-filled pores[33] has been invoked at other field sites to explain the location of pyrite and carbonate weathering fronts[34] and the OC_{petro} oxidation front[4] close to the water table.

Based on these concepts invoked to explain the pattern in absolute fluxes across the chambers (Fig. 5), some of the variability in the CO_2 fluxes at a given chamber (Fig. 3-4) could

be linked to precipitation, infiltration and runoff before or during measurements. Indeed, we see this during repeated measurements of H6 and H4 between 10/04/2019 to 10/05/2019, which experienced six short rainfall events that increased the Laval stream discharge (Extended Data Fig. 2). Each rainfall event reduced CO_2 fluxes, but they recovered over a few days (Extended Data Fig. 2). In contrast, the largest CO_2 flux occurred in mid-October 2017 after a 4-month period of drought (Fig. 3a, Extended Data Fig. 3). All chambers showed similar responses to hydrological forcing, suggesting that gas motion – into the rock for O_2, and out of the rock for CO_2 – is modulated by the degree of water saturation[4,34]. Lateral export of CO_2 as dissolved inorganic carbon[31,35] may also play a role in the CO_2 flux variability we observed. However, it cannot explain the seasonal pattern of the total CO_2 flux over 2.5-years, nor the correlation with temperature. Indeed, the near surface water content of the marls in the Laval catchment[36] is not correlated with temperature (Extended Data Fig. 4), while a month-long detailed measurements clearly shows that CO_2 emissions closely follow daily-averaged chamber temperature (Extended Data Fig. 2).

Temperature sensitivity and wider implications

The overall sensitivity of rock weathering and total CO_2 emissions to temperature is provided by the average growth exponential value α (0.070 ± 0.007 °C^{-1}) of the whole data set (Fig. 3b). This value can be used to calculate a Q_{10} factor, by which the oxidative weathering processes responsible for the CO_2 flux change as a result of a 10°C rise in temperature:

$$Q_{10} = \exp(10\alpha) \quad (2)$$

In the Laval catchment, total CO_2 release during rock weathering responds to temperature with a Q_{10} factor of 2.0 ± 0.1 over the range 0-25°C. This value is “apparent” as it is the integrated response of many biogeochemical processes, constrained by field conditions[37,38].

To explore this temperature sensitivity further, we partition the total fluxes into carbonate-derived (Reaction R3 and Reactions R7-8) and OC_{petro}-derived (Reaction R1) CO_2

using $\delta^{13}C$ and $F^{14}C$ values of the CO_2 sampled in the chambers (Methods). This assumes that ^{14}C measured in the CO_2 samples comes from atmospheric CO_2 via its dissolution as carbonic acid in rainwater (Reaction R6), which weathers carbonate as it infiltrates the shallow subsurface (Methods). In chamber H6, an average of 22 ± 6 % of the CO_2 is sourced from OC_{petro} oxidation (Reaction R1), 60 ± 6 % from $CaCO_3$ dissolution by sulfuric acid (Reaction 3), and 18 ± 9 % from $CaCO_3$ dissolution by carbonic acid (Reactions R7-8). The relatively low bicarbonate to sulfate ion ratio (~0.35) in the Laval stream water[24] supports that the $CaCO_3$ dissolution derived mostly by sulfide oxidation via H_2SO_4 following Reaction (R3), or coupled to H_2CO_3 following Reactions (R7-8). For chamber H4, the relative proportion of OC_{petro} is lower (4 ± 4 % of the total CO_2), as is the relative proportion of CO_2 produced by carbonate-dissolution by sulfuric acid (50 ± 6 %). In contrast, the proportion of H_2SO_4-induced CO_2 degassing from the dissolved inorganic carbon pool is larger (46 ± 8 %). These contrasts between H4 and H6 are intriguing, but it is difficult to draw definitive conclusions from two chambers. However, they suggest that the near-surface hydrological setting could influence the magnitude of CO_2 release (Figure 5), its short-term temporal variability (Extended Data Fig. 2) and the ultimate pathway that carbon takes from rocks to the atmosphere.

The CO_2 fluxes sourced from OC_{petro} and carbonate both vary seasonally and are positively correlated with temperature in chamber H6 (Supplementary Table 3). Over the 0-25°C range, the Q_{10} factor for sulfide oxidation coupled to carbonate dissolution is 1.7 ± 0.3 (R^2 = 0.31, p-value < 0.001, n = 27). This supports inferences from changing SO_4^{2-} concentrations of stream water in response to temperature in alpine settings[20]. The apparent activation energy (Ea) for this process is 48 ± 12 $kJ.mol^{-1}$ (R^2 = 0.53, p-value < 0.002, n = 18) for H6, which is lower than ~90 kJ/mol reported from experimental abiotic oxidation of pyrite at circumneutral pH (ref. [39]). The lower Ea we observed here in natural settings suggests that biologic processes may play a role in accelerating the kinetics of sulfide oxidation[7,40] during

rock weathering. Importantly, we show that the corresponding CO_2 release responds to temperature change.

For the oxidation of OC_{petro} in the Laval catchment, we find a Q_{10} value of 2.2 ± 0.5 (R^2 = 0.33, p-value < 0.001, n = 27). This is within uncertainty of the global median Q_{10} value of 2.4 estimated for soil respiration of recent plant-derived organic matter[41], and the mean Q_{10} of 3.0 ± 1.1 for the 0-20°C range from a global soil respiration database[38]. It is also equivalent to the value of 2.4 ± 0.3 observed for a whole-soil warming experiment[37]. Such high Q_{10} values demonstrate that the OC_{petro} in these rocks, which are type III kerogen with a moderate to low thermal maturity[25,29], is highly reactive. These Q_{10} values could reflect first order reaction kinetics, and hence occur abiotically. For OC_{petro} oxidation, apparent Ea is 45 ± 11 $kJ.mol^{-1}$ (R^2 = 0.53, p-value < 0.001, n = 18) for chamber H6. These values are lower than the lowest Ea of ~100 $kJ.mol^{-1}$ determined for abiotic thermal oxidation of sedimentary organic matter[42]. The lower Ea for OC_{petro} oxidation at our site supports that microbial activity can enhance the oxidation kinetics of OC_{petro}[42,43], as it does for plant-derived organic matter oxidation in soils[44].

Our findings challenge existing models of how chemical weathering impacts the long-term carbon cycle. At present, chemical weathering is considered a negative feedback on climate change, with silicate weathering by carbonic acid acting as a CO_2 drawdown that increases with atmospheric CO_2 concentrations (and associated temperature and runoff)[45]. The global CO_2 drawdown is estimated to be 90-120 $MtC.yr^{-1}$. For basalts, considered the most weatherable of silicate rocks, their sensitivity to temperature reveals an Ea of 42 ± 3 $kJ.mol^{-1}$ (ref. [46]) and a Q_{10} of 2.0 ± 0.2 (calculated based on data in ref. [46]). However, sedimentary rocks dominate Earth's continental surface[10,11] and global OC_{petro} oxidation[12] rates are ~40-100 MtC yr^{-1}. This CO_2 release is likely to be dominated by weathering of shales[12], with a low to moderate thermal maturity and OC_{petro} content similar to rocks at the Draix Critical Zone Observatory, rather than rocks with higher metamorphic grades[47]. Erosive landscapes like the

one studied here are likely to contribute importantly to global rates of OC_{petro} oxidation[3,17,18]. The role of temperature on oxidative weathering fluxes in locations with low denudation rate, that have deep weathering fronts[48,49] remains to be explored.

If the Q_{10} values for OC_{petro} oxidation that we measure are found to be more widespread, for a Q_{10} value of 2 (Fig. 3) a global temperature increase of 2 to 4 °C would increase the CO_2 emissions from OC_{petro} oxidation by 15% to 30%. Such imbalances in geological CO_2 emissions are unlikely to be sustained for more than ~10^6 years (ref. [50]), and thus call for the operation of the global chemical weathering thermostat to be re-examined[45]. The co-occurrence of sulfide and carbonate minerals in sedimentary rocks at the global scale, and the modern global fluxes of CO_2 release from the carbonate dissolution by sulfuric acid are less well known[8,16], but our Q_{10} values suggest that this could further enhance a positive feedback on atmospheric CO_2 concentrations associated with oxidative weathering. Overall, we propose that oxidative weathering of sedimentary rocks is a previously overlooked positive feedback that responds to global climate change. At present, such a temperature-controlled CO_2 release by OC_{petro} oxidation and/or $CaCO_3$-dissolution by sulfuric acid has not been captured in geological carbon cycle models[51]. Our data suggest that they should be, and that their temperature sensitivity should be considered alongside that of silicate weathering.

Main Text References

1. Sundquist, E. T. & Visser, K. Geologic history of the carbon cycle. in *Biogeochemistry* 425–472 (2005).
2. Petsch, S. T., Berner, R. A. & Eglinton, T. I. A field study of the chemical weathering of ancient sedimentary organic matter. in *Organic Geochemistry* **31**, 475–487 (2000).
3. Hilton, R. G. & West, A. J. Mountains, erosion and the carbon cycle. *Nat. Rev. Earth Environ.* **1**, 284–299 (2020).

4. Keller, C. K. & Bacon, D. H. Soil respiration and georespiration distinguished by transport analyses of vadose CO_2 , $^{13}CO_2$, and $^{14}CO_2$. *Global Biogeochem. Cycles* **12**, 361–372 (1998).

5. Berner, R. A. & Canfield, D. E. A new model for atmospheric oxygen over Phanerozoic time. *Am. J. Sci.* **289**, 333–361 (1989).

6. Spence, J. & Telmer, K. The role of sulfur in chemical weathering and atmospheric CO2 fluxes: Evidence from major ions, $\delta^{13}C_{DIC}$, and $\delta^{34}S_{SO4}$ in rivers of the Canadian Cordillera. *Geochim. Cosmochim. Acta* **69**, 5441–5458 (2005).

7. Calmels, D., Gaillardet, J., Brenot, A. & France-Lanord, C. Sustained sulfide oxidation by physical erosion processes in the Mackenzie River basin: Climatic perspectives. *Geology* **35**, 1003 (2007).

8. Torres, M. A., West, A. J. & Li, G. Sulphide oxidation and carbonate dissolution as a source of CO_2 over geological timescales. *Nature* **507**, 346–349 (2014).

9. Berner, E. K. & Berner, R. A. *Global environment: Water, air, and geochemical cycles*. *Global Environment: Water, Air, and Geochemical Cycles (Second Edition)* (2012).

10. Hartmann, J. & Moosdorf, N. The new global lithological map database GLiM: A representation of rock properties at the Earth surface. *Geochemistry, Geophys. Geosystems* **13**, 1–37 (2012).

11. Copard, Y., Amiotte-Suchet, P. & Di-Giovanni, C. Storage and release of fossil organic carbon related to weathering of sedimentary rocks. *Earth Planet. Sci. Lett.* **258**, 345–357 (2007).

12. Petsch, S. T. Weathering of Organic Carbon. in *Treatise on Geochemistry* **12**, 217–238 (Elsevier, 2014).

13. Burke, A. *et al.* Sulfur isotopes in rivers: Insights into global weathering budgets,

pyrite oxidation, and the modern sulfur cycle. *Earth Planet. Sci. Lett.* **496**, 168–177 (2018).

14. Plank, T. & Manning, C. E. Subducting carbon. *Nature* **574**, 343–352 (2019).

15. Hedges, J. I. & Keil, R. G. Sedimentary organic matter preservation: an assessment and speculative synthesis. *Mar. Chem.* **49**, 81–115 (1995).

16. Torres, M. A., Moosdorf, N., Hartmann, J., Adkins, J. F. & West, A. J. Glacial weathering, sulfide oxidation, and global carbon cycle feedbacks. *Proc. Natl. Acad. Sci.* **114**, 8716–8721 (2017).

17. Hilton, R. G., Gaillardet, J., Calmels, D. & Birck, J. L. Geological respiration of a mountain belt revealed by the trace element rhenium. *Earth Planet. Sci. Lett.* **403**, 27–36 (2014).

18. Horan, K. *et al.* Mountain glaciation drives rapid oxidation of rock-bound organic carbon. *Sci. Adv.* **3**, e1701107 (2017).

19. Bufe, A. *et al.* Co-variation of silicate, carbonate and sulfide weathering drives CO_2 release with erosion. *Nat. Geosci.* **14**, 211–216 (2021).

20. Crawford, J. T., Hinckley, E.-L. S., Litaor, M. I., Brahney, J. & Neff, J. C. Evidence for accelerated weathering and sulfate export in high alpine environments. *Environ. Res. Lett.* **14**, 124092 (2019).

21. Soulet, G. *et al.* Technical note: In situ measurement of flux and isotopic composition of CO_2 released during oxidative weathering of sedimentary rocks. *Biogeosciences* **15**, 4087–4102 (2018).

22. Mathys, N., Brochot, S., Meunier, M. & Richard, D. Erosion quantification in the small marly experimental catchments of Draix (Alpes de Haute Provence, France). Calibration of the ETC rainfall–runoff–erosion model. *CATENA* **50**, 527–548 (2003).

23. Gaillardet, J. *et al.* OZCAR : The French Network of Critical Zone Observatories.

(2018). doi:10.2136/vzj2018.04.0067

24. Cras, A., Marc, V. & Travi, Y. Hydrological behaviour of sub-Mediterranean alpine headwater streams in a badlands environment. *J. Hydrol.* **339**, 130–144 (2007).

25. Graz, Y. *et al.* Annual fossil organic carbon delivery due to mechanical and chemical weathering of marly badlands areas. *Earth Surf. Process. Landforms* **37**, 1263–1271 (2012).

26. Maquaire, O. *et al.* Caractérisation des profils de formations superficielles par pénétrométrie dynamique à énergie variable : application aux marnes noires de Draix (Alpes-de-Haute-Provence, France). *Comptes Rendus Geosci.* **334**, 835–841 (2002).

27. Lofi, J. *et al.* Geological discontinuities, main flow path and chemical alteration in a marly hill prone to slope instability: Assessment from petrophysical measurements and borehole image analysis. *Hydrol. Process.* **26**, 2071–2084 (2012).

28. Husson, J. M. & Peters, S. E. Atmospheric oxygenation driven by unsteady growth of the continental sedimentary reservoir. *Earth Planet. Sci. Lett.* **460**, 68–75 (2017).

29. Copard, Y., Di-Giovanni, C., Martaud, T., Albéric, P. & Olivier, J.-E. Using Rock-Eval 6 pyrolysis for tracking fossil organic carbon in modern environments: implications for the roles of erosion and weathering. *Earth Surf. Process. Landforms* **31**, 135–153 (2006).

30. Oertel, C., Matschullat, J., Zurba, K., Zimmermann, F. & Erasmi, S. Greenhouse gas emissions from soils—A review. *Geochemistry* **76**, 327–352 (2016).

31. Winnick, M. J. *et al.* Snowmelt controls on concentration-discharge relationships and the balance of oxidative and acid-base weathering fluxes in an alpine catchment, East River, Colorado. *Water Resour. Res.* **53**, 2507–2523 (2017).

32. Tune, A. K., Druhan, J. L., Wang, J., Bennett, P. C. & Rempe, D. M. Carbon Dioxide Production in Bedrock Beneath Soils Substantially Contributes to Forest Carbon

Cycling. *J. Geophys. Res. Biogeosciences* **125**, (2020).

33. Feng, G., Wu, L. & Letey, J. Evaluating aeration criteria by simultaneous measurement of oxygen diffusion rate and soil-water regime. *Soil Sci.* **167**, 495–503 (2002).

34. Brantley, S. L., Holleran, M. E., Jin, L. & Bazilevskaya, E. Probing deep weathering in the Shale Hills Critical Zone Observatory, Pennsylvania (USA): the hypothesis of nested chemical reaction fronts in the subsurface. *Earth Surf. Process. Landforms* **38**, 1280–1298 (2013).

35. Duvert, C., Butman, D. E., Marx, A., Ribolzi, O. & Hutley, L. B. CO2 evasion along streams driven by groundwater inputs and geomorphic controls. *Nat. Geosci.* **11**, 813–818 (2018).

36. Mallet, F. *et al.* Assessing soil water content variation in a small mountainous catchment over different time scales and land covers using geographical variables. *J. Hydrol.* **591**, 125593 (2020).

37. Hicks Pries, C. E., Castanha, C., Porras, R. C. & Torn, M. S. The whole-soil carbon flux in response to warming. *Science* **355**, 1420–1423 (2017).

38. Bond-Lamberty, B. & Thomson, A. A global database of soil respiration data. *Biogeosciences* **7**, 1915–1926 (2010).

39. Nicholson, R. V., Gillham, R. W. & Reardon, E. J. Pyrite oxidation in carbonate-buffered solution: 1. Experimental kinetics. *Geochim. Cosmochim. Acta* **52**, 1077–1085 (1988).

40. Percak-Dennett, E. *et al.* Microbial acceleration of aerobic pyrite oxidation at circumneutral pH. *Geobiology* **15**, 690–703 (2017).

41. Raich, J. W. & Schlesinger, W. H. The global carbon dioxide flux in soil respiration and its relationship to vegetation and climate. *Tellus B* **44**, 81–99 (1992).

42. Hemingway, J. D. *et al.* Microbial oxidation of lithospheric organic carbon in rapidly eroding tropical mountain soils. *Science* **360**, 209–212 (2018).

43. Petsch, S. T., Eglinton, T. I. & Edwards, K. J. 14C-Dead Living Biomass: Evidence for Microbial Assimilation of Ancient Organic Carbon During Shale Weathering. *Science* **292**, 1127–1131 (2001).

44. Leifeld, J. & von Lützow, M. Chemical and microbial activation energies of soil organic matter decomposition. *Biol. Fertil. Soils* **50**, 147–153 (2014).

45. Maher, K. & Chamberlain, C. P. Hydrologic Regulation of Chemical Weathering and the Geologic Carbon Cycle. *Science* **343**, 1502–1504 (2014).

46. Li, G. *et al.* Temperature dependence of basalt weathering. *Earth Planet. Sci. Lett.* **443**, 59–69 (2016).

47. Galy, V., Beyssac, O., France-Lanord, C. & Eglinton, T. Recycling of Graphite During Himalayan Erosion: A Geological Stabilization of Carbon in the Crust. *Science* **322**, 943–945 (2008).

48. Gu, X., Heaney, P. J., Reis, F. D. A. A. & Brantley, S. L. Deep abiotic weathering of pyrite. *Science* **370**, eabb8092 (2020).

49. Jin, L. *et al.* The CO2 consumption potential during gray shale weathering: Insights from the evolution of carbon isotopes in the Susquehanna Shale Hills critical zone observatory. *Geochim. Cosmochim. Acta* **142**, 260–280 (2014).

50. Berner, R. A. & Caldeira, K. The need for mass balance and feedback in the geochemical carbon cycle. *Geology* **25**, 955 (1997).

51. Caves Rugenstein, J. K., Ibarra, D. E. & von Blanckenburg, F. Neogene cooling driven by land surface reactivity rather than increased weathering fluxes. *Nature* **571**, 99–102 (2019).

Acknowledgements: This research was funded by a European Research Council Starting Grant to RGH (ROC-CO2 project, grant 678779). Radiocarbon measurements were funded by the Natural Environment Research Council (NERC), UK (Allocation 2074.1017) to GS, RGH and MHG. We thank staff at NERC RCF and SUERC. We thank Clément Flaux and Anne-Eléonore Paquier for field assistance in Dec. 2016. This study was carried out in Draix-Bleone Observatory (France) and used its infrastructure and temperature and river discharge data. Draix-Bleone Observatory is funded by INRAE, INSU and OSUG and is part of OZCAR Research Infrastructure that is supported by the French Ministry of Research, French Research Institutions and Universities.

Author contribution statement: RGH conceived the research and designed the study with GS. GS and SK built and maintained the chambers. GS and RGH carried out fieldwork with additional assistance from TR, TC and MD. GS led the CO_2 flux measurements and all related calculations and analysis. SK collected and provided field temperature data, discharge and precipitation data. MHG provided materials for sampling CO_2 for isotopic analyses. GS and MHG carried out geochemical analyses. GS and RGH analysed the results. GS and RGH wrote the paper with inputs from all co-authors.

Competing interest statement: We declare no competing interest.

Figures legends/captions

Figure 1: The Laval field site. a: Chambers H4, H6, H7, H8 and H13 were installed, alongside the chamber for the temperature probe, in Callovo-Oxfordian marls. The operator (silhouette, ~185 cm) is measuring CO_2 flux in chamber H6 with a CO_2 analyser connected to the MS^3 (molecular sieve sampling system; ref. [52]). **b**: View of H7 and H8 (dashed white square in a), with H7 installed in bedrock below the surface soil. **c**: The chamber design[21] for H6, with white PVC tubing to be inserted at the outlet. Bottom picture shows the rubber stopper fitted in the PVC tubing. Two glass tubes go through the rubber stopper and are fitted with Tygon® tubing, sealed with the red clips, and the exterior of the chamber is sealed with outdoor sealant. **d**: Schematic diagram of the closed-loop MS^3 connected to the chamber. Gas flow pathways (blue arrows) are controlled by opening and closing the clips (red bars) to measure CO_2 concentration (via the bypass) and scrub CO_2 (soda lime) or trap a CO_2 sample (zeolite molecular sieve).

Figure 2: The source of CO_2 sampled from chambers H4 and H6 based on its isotopic composition. Radiocarbon composition ($F^{14}C$) *versus* stable carbon isotopes ($\delta^{13}C$) of the CO_2 samples from H4 and H6 (circles). End-member values were assessed from direct measurements of atmospheric CO_2 in the Laval catchment (Draix, France) (black crosses), carbonates (blue crosses) and rock organic carbon (OC_{petro}; brown crosses) contained in the Jurassic marls. The chamber CO_2 samples show a high proportion of geologic carbon (low $F^{14}C$), implying only a small contribution from atmospheric CO_2. $\delta^{13}C$ values are generally closer to the carbonate endmember, showing that chamber CO_2 is mostly sourced by carbonate dissolution by sulfuric acid. Radiocarbon can be sourced from atmospheric CO_2 via carbonic acid weathering of carbonate (Reactions R6-8) and/or leaks during sample collection (Methods).

Figure 3: Measured total CO_2 emissions from rock weathering in the Laval catchment (Draix, France) for 2.5 years from late December 2016 to early May 2019. **a:** Total CO_2 flux (carbonate-derived and OC_{petro}-derived) measured in chambers H4 and H6 compared to the temperature measured in the rock interior (black line [daily temperature average] and grey envelope [daily amplitude]; Methods). **b:** Total CO_2 flux measured in chambers H4, H6, H7, H8, H13 normalized to their amplitude parameter (F_0) (Methods and Supplementary Table 2) compared to temperature measured in the rock interior. Error bars indicate standard deviation on the flux measurements (Methods) when larger than the symbol size.

Figure 4: Temperature sensitivity of total CO_2 release by sedimentary rock weathering. Growth exponential fits of the CO_2 flux versus temperature in the rock interior: $y = F_0 exp(\alpha x)$. **a:** Individual fits on the data for chambers H4 and H6 (bold lines) and their 1σ envelope (dashed lines). **b:** Fit (bold line) on all CO_2 flux measured in chambers H4, H6, H7, H8, H13 normalized to their amplitude parameter (F_0) (Methods and Supplementary Table 2) and its 1σ envelope (dashed lines). Q_{10} thermal factor is $exp(10\alpha)$. Statistics on each fit are available in Supplementary Table 2. Error bars indicate standard deviation on the flux measurements, when larger than the symbol size (Methods).

Figure 5: Variability in the total CO_2 emissions compared to the elevation of the rock chambers above the Laval river bed. Box plots show the full measured variability in each chamber (H4, H6, H7, H8, and H13), the minimum value, the 25th percentile, the median, the 75th percentile, the maximum value and outliers (crosses). Dashed line (– · –) is the elevation *versus* CO_2 flux median linear fit (r^2 = 0.98; *p-value* < 0.001). Symbols are the amplitude parameter F_0 (Methods and Supplementary Table 2) obtained through the growth exponential fits on data for each chamber. Error bars show 1σ uncertainty on the amplitude parameter.

Dashed line (- -) is the elevation *versus* amplitude parameter linear fit (r^2 = 0.98; *p-value* < 0.001). See Supplementary Tables 2 and 4 for numerical values.

Methods

Field area. The Laval catchment (Draix, France) in the Draix-Bléone observatory is located in the French southern Alps, part of OZCAR the French network of observatories for the study of the critical zone[23]. The Laval catchment (0.86 km^2; altitude between 800 and 1250 m) is a headwater catchment that has been instrumented since 1982 to monitor rainfall, water discharge, suspended load and bedload transport[22,53,54]. Meteorological data including air temperature and humidity are also continuously recorded[53,54].

The Laval catchment is composed of finely bedded, mechanically weak and erodible Jurassic black marls (Bathonian, Callovian and lower Oxfordian ages). From 1985 to 2016, mean annual rainfall was 916 ± 175 mm. The catchment is characterized by a Mediterranean climate with a hot and dry summer. During summer, rain events occur during abrupt, short and intense thunderstorms. Spring and autumn are characterized by rain of lower intensity but lasting up to several days. It is also a mountain climate with freeze-thaw cycles during wintertime. The combination of freeze-thaw and wet-dry cycles are important in the physical weathering of marls[22,54], and combined with the intense precipitation, incised channels and steep hillslopes, leads to high erosion rates of 7 to 10 mm/yr (ref. [21,22,25]).

These conditions limit the development of soils but favour the development of a dense gully network typical of badlands. The catchment is sparsely vegetated with marls outcropping as bare rock over 68% of the catchment surface area (0.58 km^2) (refs. [22,24]). It is thus easy to find regolith and rocks that are devoid of soils and roots (Fig. 1a). Bare rock outcrops are characterized by partly weathered marls and regolith. Regolith is generally ~20 cm deep: the upper ~3 cm is a loose detrital cover composed of cm-sized fragments of marls; from ~3 to 10 cm is the loosened somewhat fragmented upper regolith; from ~10 to ~20 cm is the compact lower regolith; below is the unweathered marl bedrock[22,26]. Lateral variation in the regolith

thickness is usually observed with larger thickness on crests, intermediate in gullies and minimal in talwegs[26].

In situ rock weathering chambers. The experimental setup has been detailed previously[21]. Here in summary, each chamber is drilled directly into the rock with a rock drill. The rock face is cleared before drilling. Rock powder left inside the chamber after drilling is blown away with a pressurized air gun. The entrance of the chamber is fitted with a ~3cm-long PVC tube, in which a rubber stopper is inserted. Two glass tubes are inserted through the rubber stopper (Fig. 1). The external parts of the glass tubes that stick out of the stopper are fitted with Tygon® tubing. In order to isolate the chamber from the atmosphere, the Tygon® tubing is clipped, and silicon sealant is placed around the entrance of the chamber. The inside wall of the chamber is the exchange surface area between the rock pore space and chamber headspace, and through which the rock CO_2 emission passes. We designed the chamber dimensions (40 cm deep and 3 cm diameter) so that the ratio surface/volume is large, benefitting CO_2 flux measurements. Chambers are stable, required little maintenance, and stayed in the field for the entire experiment making it possible to monitor CO_2 emissions over seasonal cycles.

Five chambers were installed in barren marls on the left side of the Laval river (N44.1406, E06.3628) within a distance of 12 metres on the North-facing side of the Laval stream valley (Figure 1a). Chamber H7 is located 1.27 m above the river bed and 0.46 m above chamber H8. Seven metres upstream, chamber H13 was installed at an elevation 1.90 m above the river bed. Another five metres upstream, chamber H6 was installed at an elevation of 2.31 m above the river bed, and 0.98 m above chamber H4.

In this study, we present data from a set of 5 chambers that had the same aspect; were on the same rock outcrop; had no roots present; remained well sealed; and were not destroyed

quickly by flooding or wild animals. Other chambers were drilled that were not included here because they were either: test chambers from a reconnaissance field trip (H1-3); had a poor seal (H5); as a dummy chamber for a temperature probe (H12); drilled on a south facing slope partly in colluvium (H9-11 and H14). After the ~2.5-year long experiment, all chamber materials were removed from the field site.

Flux measurements. Flux measurements and calculations were described previously in ref. [21]. In summary, to measure the CO_2 flux, the chamber is connected to an infra-red gas analyser (EGM 5 Portable CO_2 Gas Analyzer, PP Systems, USA) using the molecular sieve sampling system (MS^3) described in ref. [52]. This allows the operator to first bring the chamber CO_2 concentration to ~400 ppm of the local atmosphere (using soda lime or a zeolite material to remove CO_2 from the chamber), before then recording the CO_2 accumulation in the chamber over time. During each field visit, we typically recorded a sequence of *n* repeats of 5-minute-long accumulations of CO_2 for each chamber. The number of repeats (*n*) was at least 7 but usually 8 or more. From one sequence, we calculated *n* rates (q_i) of CO_2 accumulation ($\mu gC.min^{-1}$) fitting the data with the exponential model described in ref. [55] over a fitting window of 3.5 minutes after CO_2 concentration typically reaches ~400 ppm in the chamber. The first 3 measurements of CO_2 accumulation are used to purge the CO_2 that accumulated in the rock pore space around the chamber during the hours before measurements. Hence, the first 3 calculated rates were excluded, and we calculated an average CO_2 accumulation rate for the chamber:

$$\bar{q} = \frac{1}{n-3}\sum_{4}^{n} q_i \qquad (3)$$

We take this value as representative of the rate at which CO_2 evades from the naturally fractured, porous rock mass at the time of the sequence of the repeated measurements. The

uncertainty on the average rate was taken as the standard deviation of the *n*-3 considered individual rates. From these series we also calculated a scaling factor (A) for each sequence:

$$A = {}^{\bar{q}}/_{q_1} \quad (4)$$

For each chamber, over 2.5 years we obtained an averaged factor $\bar{A}$ and its standard deviation. For some of the measurement sequences we did not manage to measure a full series of at least 7 repeats. In this case the CO_2 flux was obtained by scaling the very first repeat using parameter $\bar{A}$. In that case, the average $\bar{q}$ was calculated as follows:

$$\bar{q} = q_1 \times \bar{A} \quad (5)$$

Standard deviation of $\bar{A}$ was propagated to provide an uncertainty on the scaled rate. Finally, we converted each obtained CO_2 accumulation rate $\bar{q}$ (µgC.min^{-1}) into a CO_2 flux (F) (mgC.m^{-2}.day^{-1}) using the internal surface area (S) of the considered chamber:

$$F = 1440\,\bar{q}/S \quad (6)$$

To test whether our approach (chambers drilled in the rock) yields comparable CO_2 fluxes to more traditional surface chambers, we installed two short-term surface chambers in October 2017. The chambers were plastic boxes (length = 19.5 cm, width = 8.2 cm and height = 3.5 cm) which were sealed to the rock face with silicone sealant two days before measurements were made. These were located on the same outcrop as the drilled rock chambers, at a similar elevation above the river channel to chamber H8. The measured fluxes on 12/10/2017 (determined in the same way as our rock-chambers, with pCO_2 lowered to ambient atmosphere, and then left to build up) were 138 ± 14 mgC m^{-2} day^{-1} for surface chamber W01, and 241 ± 13 mgC m^{-2} day^{-1} for surface chamber B02. During the same sampling trip (with a temperature of between 10 and 11°C in the rock during measurement), these fluxes are consistent with those measured for Chamber H8 (191± 39 mgC m^{-2} day^{-1}) at a similar relative elevation above the river channel, and slightly lower than that measured for Chamber H7 (323 ± 85 mgC m-2 day^{-}

[1]) which is located at a higher elevation. These are small offsets in the context of the environmental controls on the flux that change the flux by a factor of 2 over 10 degrees. Therefore, our method yields results comparable to more traditional surface chambers. The advantage of the rock chambers is their: i) large surface area to volume ratio, meaning CO_2 could be trapped more efficiently for isotopic analysis; ii) longevity, allowing us to revisit the same substrate at each field visit.

CO_2 isotopic composition. After measuring the CO_2 accumulation in the chamber, the MS^3 enables the operator to trap the CO_2 gas in zeolite molecular sieves (type 13X) (ref. [21,52]). The CO_2 samples trapped from the chambers were extracted from the zeolite molecular sieve in the laboratory by heating. Extracted CO_2 is then purified cryogenically under vacuum[56]. An aliquot of the CO_2 sample is used to measure its stable carbon isotopic composition ($\delta^{13}C$) by Isotopic Ratio Mass Spectrometry (Thermo Fisher Delta V; results expressed relative to the Vienna Pee Dee Belemnite (VPDB) standard). A further aliquot was graphitized to measure its radiocarbon (^{14}C) concentration by Accelerator Mass Spectrometry at the Scottish Universities Environmental Research Centre (SUERC). Following convention, ^{14}C measurements were corrected for isotopic fractionation using the measured sample IRMS $\delta^{13}C$ values, and reported in the form of the fraction modern, i.e., the $F^{14}C$ notation[57].

We collected atmospheric CO_2 samples using the MS^3 coupled to the CO_2 gas analyser by circulating atmospheric air through the zeolite. Atmospheric CO_2 was extracted and analysed for its isotopic composition as described above.

Carbon isotope composition and contents of the rock. After having drilled the chamber, we sampled the powdered rock for inorganic and organic carbon analysis. Samples were freeze-dried and crushed to fine powder. Total carbon (TC) and Inorganic carbon (IC) content of the

rock samples were obtained using an elemental analyser (Jena Multi EA 4000). Rock organic carbon content was obtained by difference (OC_{petro} = TC – IC). Carbon contents are reported in % weight. Stable carbon isotope composition of the rock organic carbon (OC_{petro}) was obtained using a Costech Elemental Analyser coupled to a Thermo Delta V Isotope Ratio Mass Spectrometer (IRMS) run with normalising standards (international and internal) and external standards to check precision and accuracy. Stable carbon isotope of the rock inorganic carbon was obtained using a carbonate dissolution device (Thermo Gas Bench II) coupled to an IRMS (ThermoScientific MAT 253). Stable carbon isotopes ($\delta^{13}C$) are reported in ‰ compared to the VPDB standard.

Mixing model for source of CO_2. We assume that the isotopic composition of the trapped CO_2 reflects a three-component mixture of carbon:

$$\begin{bmatrix} 1 & 1 & 1 \\ \delta^{13}C_{OC} & \delta^{13}C_{SA} & \delta^{13}C_{CA} \\ F^{14}C_{OC} & F^{14}C_{SA} & F^{14}C_{CA} \end{bmatrix} \cdot \begin{bmatrix} f_{OC} \\ f_{SA} \\ f_{CA} \end{bmatrix} = \begin{bmatrix} 1 \\ \delta^{13}C_{Ch} \\ F^{14}C_{Ch} \end{bmatrix} \quad (7)$$

where f is the mass fraction of CO_2 sourced by the oxidation of the rock organic carbon (f_{OC}; Reaction R1), the dissolution of carbonate minerals by sulfuric acid (f_{SA}; Reactions R2-3), and the dissolution of carbonate minerals by carbonic acid coupled to sulfuric-acid-driven degassing (f_{CA}; Reactions R6-8)). Subscript “Ch” stands for the CO_2 sampled from the chambers. The terms $\delta^{13}C$ and $F^{14}C$ stand for the stable carbon isotope and radiocarbon compositions of the three possible sources of CO_2 listed above and of the CO_2 sampled in the chamber.

The $\delta^{13}C$ and $F^{14}C$ values are based on the chemical reactions (Eq. (1), (3) and (6-8)), on the fractionation factor Δ between bicarbonate and CO_2 (ref. [58]), and on measurements of OC_{petro}, $CaCO_3$, and atmospheric CO_2 sampled from the from the field site (Supplementary

Information). The $F^{14}C$ of $CaCO_3$ and OC_{petro} are assumed to be 0 (ref. [21]). For the oxidation of rock organic carbon, Reaction (R1) yields:

$$\delta^{13}C_{OC} = \delta^{13}C_{OC_{petro}} \quad (8)$$

$$F^{14}C_{OC} = F^{14}C_{OC_{petro}} = 0 \quad (9)$$

For the dissolution of carbonate minerals by sulfuric acid, Reaction (R3) yields:

$$\delta^{13}C_{SA} = \delta^{13}C_{CaCO_3} \quad (10)$$

$$F^{14}C_{SA} = F^{14}C_{CaCO_3} = 0 \quad (11)$$

For the dissolution of carbonate minerals by carbonic acid coupled to CO_2 degassing driven by sulfuric acid, Reactions (R6-8) yields:

$$\delta^{13}C_{CA} = \frac{1}{2}\left(\delta^{13}C_{atm} + \Delta + \delta^{13}C_{CaCO_3}\right) - \Delta \quad (12)$$

$$F^{14}C_{CA} = \frac{1}{2}\left(F^{14}C_{atm} + F^{14}C_{CaCO_3}\right) = \frac{1}{2}F^{14}C_{atm} \quad (13)$$

Errors on the results were calculated based on a Monte-Carlo simulation of error propagation using the standard deviation of the measured $\delta^{13}C$ and $F^{14}C$ of the end-members and CO_2 sampled in the chambers.

The mixing approach assumes that the ^{14}C-enrichment comes from atmospheric CO_2 dissolved in rain, which is consistent with the higher $F^{14}C$ values of the CO_2 sampled from chamber H4 located close to the water table, compared to the CO_2 with lower $F^{14}C$ values sampled from chamber H6 located away from the water table (Fig. 2 and 5) .

Alternatively, the ^{14}C enrichment may occur through the weathering of silicate minerals by carbonic acid coupled to the degassing of CO_2 driven by sulfuric acid (Reaction R8):

$$CaSiO_3 + 2H_2CO_3 \rightarrow Ca^{2+} + 2HCO_3^- + H_2O + SiO_{2,aq} \quad (R9)$$

However, as the kinetics of dissolution of silicate minerals are slower than those of carbonate[59], in rapidly eroding settings, this pathway is likely to be of second order importance compared to the dissolution of carbonates. This is corroborated by the chemistry of the Laval river waters

yielding very low bicarbonate-to-sulfate ratio (0.35; ref. [24,60]) compatible with that of 0 resulting from the two carbonate dissolution pathways Reaction (R3) and (R7-8).

Natural leaks around the chamber entrance, or within the gas sampling case[21,52] could also explain the ^{14}C enrichment of the sampled CO_2. However, the pCO_2 in the chambers was always higher, sometimes by thousands of part per million, than that of the atmosphere. Thus, the CO_2 must diffuse out of the rock face towards the atmosphere, and atmospheric contamination from leaks around the chamber entrance should be minor.

Activation energy (Ea). Arrhenius equation relates the rate of a reaction k (here a CO_2 flux) to the absolute temperature (T in Kelvin), gas constant (R), a pre-exponential factor A and the activation energy of the reaction (Ea):

$$k = Ae^{\frac{-Ea}{RT}} \quad (9)$$

Rearranging the logarithm of equation (14) yields:

$$-R \times \ln(k) = -R \times \ln(A) + {}^{Ea}/_{T} \quad (15)$$

Equation (15) has the form of a linear equation ($y = b + mx$) where y is -R×ln(k) and x is 1/T, with the slope m being the activation energy (Ea). Thus, linear fitting - R×ln(k) as a function of 1/T returns Ea.

Environmental data. Since 2000, the air temperature is recorded every 10 minutes using a HMP45C temperature and relative humidity probe (Campbell Scientific Inc.) at the "Le Plateau" automated weather station. The weather station is located at the outlet of the Laval catchment, at the same elevation and 200 metres from the field area where headspace chambers were installed.

In order to estimate the temperature inside the chambers, we drilled a chamber on the same outcrop (Fig. 1). On 12/10/2017, this chamber was equipped with a PT100 temperature sensor (Campbell Scientific Inc.) coupled to a CR1000 control datalogger (Campbell Scientific Inc.). The temperature sensor was inserted into the chamber through the rubber stopper. Then we sealed the chamber to insulate it from the exterior. Temperature was recorded every 5 minutes. We considered this temperature record as representative of the rock temperature for all the chambers located on the same outcrop (H4, H6, H13, H7 and H8). We could not record chamber temperature for almost 10 months from 14/12/2016 to 11/10/2017, a period that includes the four first field trips. Instead we reconstructed the chamber temperature from the "Le Plateau" air temperature using a calibration curve. The calibration is based on a 12-month period of overlap between temperature recorded in the chamber and the air temperature recorded at the "Le Plateau" weather station, from 13/10/2017 and 24/10/2018. Over this period, we return a significant correlation (Fourier model; $R^2 = 0.97$; p-value < 0.001; n = 377; Extended Data Fig. 5-6) between the daily average temperature measured on day "d" in the chamber ($T_{chamber,\ d}$) and factor γ, which we defined as the air temperature averaged over a 3-days window preceding day "d", and weighed by the fractional duration of daylight (L) at the Laval catchment latitude:

$$\gamma = \frac{1}{3}\sum_{i\,=\,d-3}^{i\,=\,d-1}\left[T_{air,i} \times L_i\right] \qquad (16)$$

Weighting the air temperature by the fractional duration of daylight approximately accounts for the duration of exposure of the outcrop to daylight.

At the outlet of the Laval catchment, the river water discharge is continuously recorded at a gauging station equipped with a calibrated flume (Parshall flume) and two level recorders (ultrasonic sensor and numerical rule) (ref. [54]).

Method references

52. Hardie, S. L. M. L., Garnett, M. H. H., Fallick, A. E., Rowland, A. P. & Ostle, N. J. J. Carbon Dioxide Capture Using a Zeolite Molecular Sieve Sampling System for Isotopic Studies (13C and 14C) of Respiration. *Radiocarbon* **47**, 441–451 (2005).

53. Draix-Bléone Observatory. Observatoire hydrosédimentaire de montagne Draix-Bleone [Data Set]. Irstea. (2015). doi.org/10.17180/obs.draix

54. Mathys, N. & Klotz, S. Draix: A field laboratory for research on hydrology and erosion in mountain areas. *Proc. 4th Can. Conf. Geohazards From Causes to Manag.* 594 (2008).

55. Pirk, N. *et al.* Calculations of automatic chamber flux measurements of methane and carbon dioxide using short time series of concentrations. *Biogeosciences* **13**, 903–912 (2016).

56. Garnett, M. H. & Murray, C. Processing of CO2 Samples Collected Using Zeolite Molecular Sieve for 14C Analysis at the NERC Radiocarbon Facility (East Kilbride, UK). *Radiocarbon* **55**, 410–415 (2013).

57. Reimer, P. J., Brown, T. A. & Reimer, R. W. Discussion: Reporting and Calibration of Post-Bomb 14C Data. *Radiocarbon* **46**, 1299–1304 (2004).

58. Mook, W. G., Bommerson, J. C. & Staverman, W. H. Carbon isotope fractionation between dissolved bicarbonate and gaseous carbon dioxide. *Earth Planet. Sci. Lett.* **22**, 169–176 (1974).

59. Tipper, E. T. *et al.* The short term climatic sensitivity of carbonate and silicate weathering fluxes: Insight from seasonal variations in river chemistry. *Geochim. Cosmochim. Acta* **70**, 2737–2754 (2006).

60. Marc, V. *et al.* Groundwater-Surface waters interactions at slope and catchment scales: implications for landsliding in clay-rich slopes. *Hydrol. Process.* **31**, 364–381 (2017).

Data availability

All data that support the findings of this study are available from the Natural Environment Research Council (NERC) – British Geological Survey (BGS) National Geoscience Data Centre with the identifier https://doi.org/10.5285/efc082aa-5c2b-4afb-aec8-344aebaea653

Code availability

Custom Matlab® codes and accompanying pCO_2 source data are available on request from the corresponding authors.

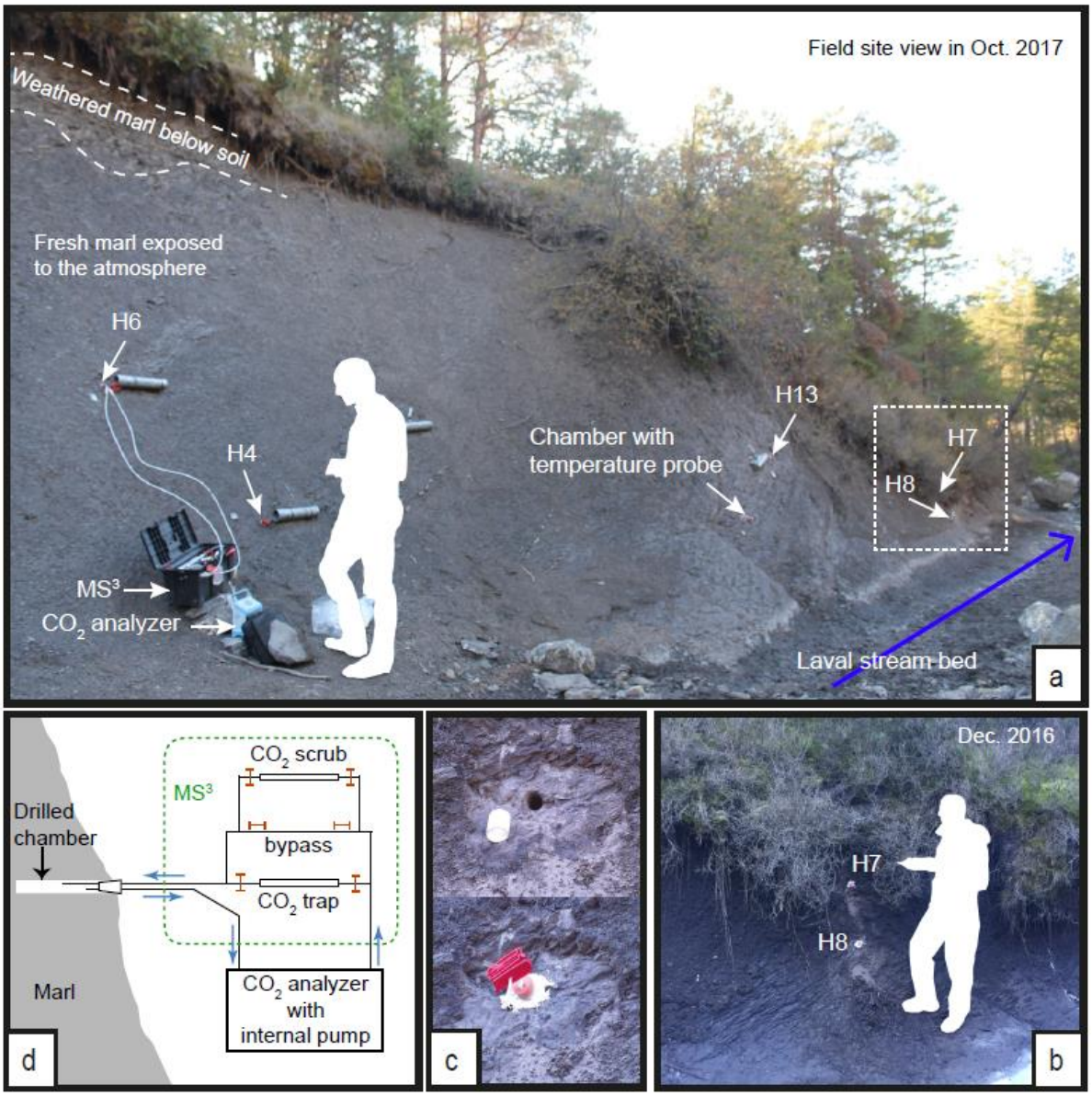
Field site view in Oct. 2017
Weathered marl below soil
Fresh marl exposed to the atmosphere
H6
H4
MS³
CO₂ analyzer
Chamber with temperature probe
H13
H7
H8
Laval stream bed
a
CO₂ scrub
MS³
Drilled chamber
bypass
CO₂ trap
Marl
CO₂ analyzer with internal pump
d
c
Dec. 2016
H7
H8
b

Figure 1

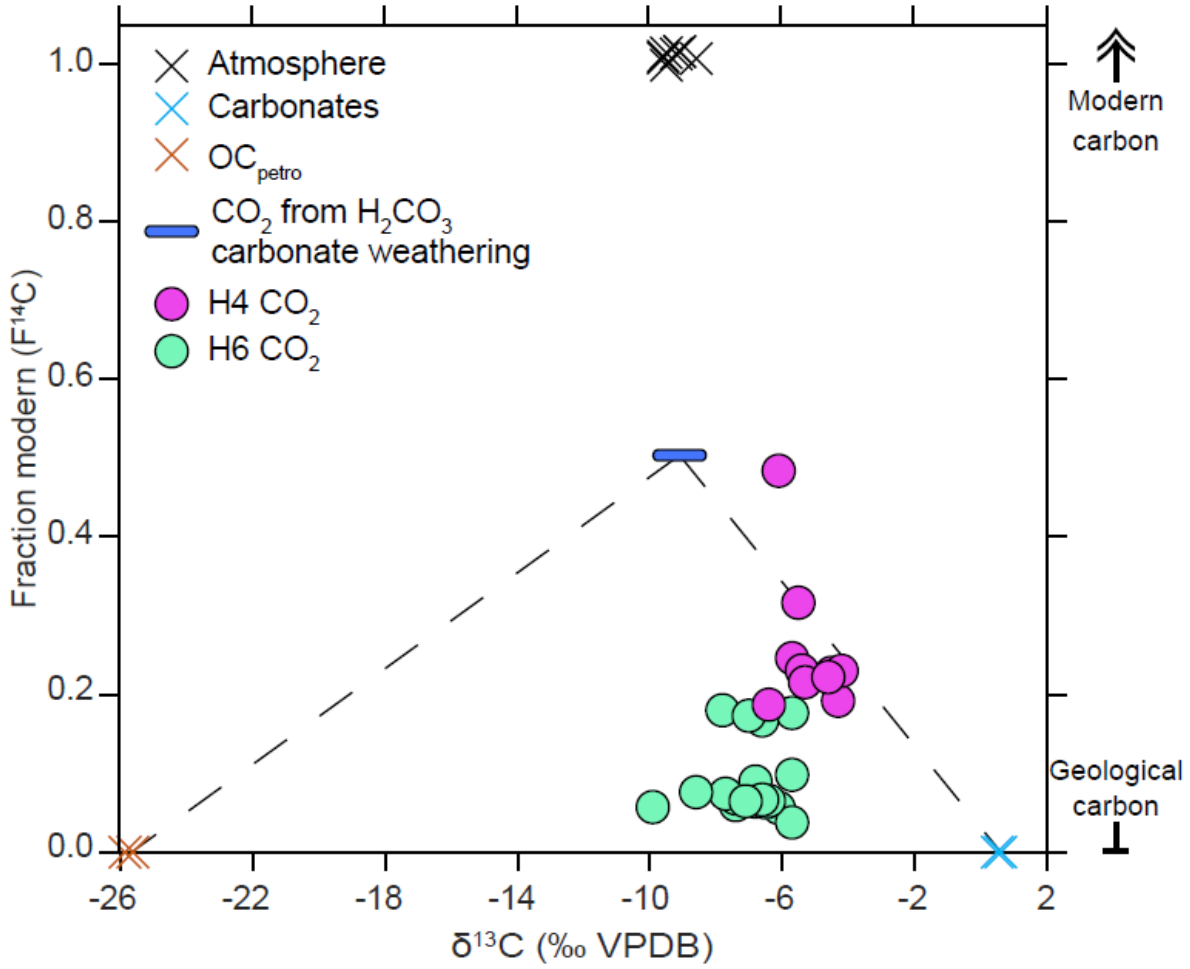
Atmosphere
Carbonates
OC petro
CO2 from H2CO3 carbonate weathering
H4 CO2
H6 CO2
Modern carbon
Geological carbon
Fraction modern (F14C)
δ13C (‰ VPDB)
1.0
0.8
0.6
0.4
0.2
0.0
-26
-22
-18
-14
-10
-6
-2
2

Figure 2

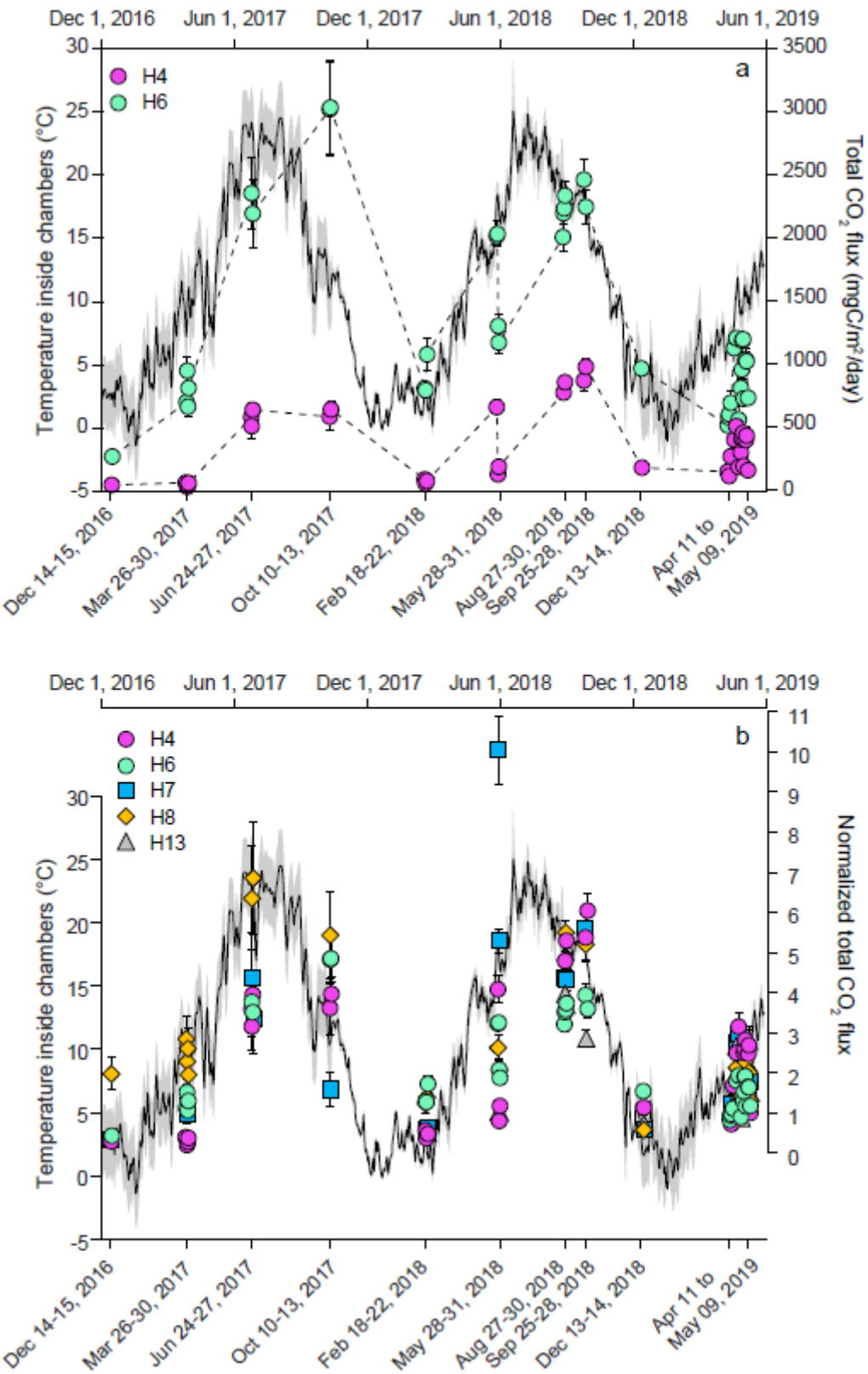
Dec 1, 2016
Jun 1, 2017
Dec 1, 2017
Jun 1, 2018
Dec 1, 2018
Jun 1, 2019
a
H4
H6
Temperature inside chambers (°C)
Total CO2 flux (mgC/m²/day)
Dec 14-15, 2016
Mar 26-30, 2017
Jun 24-27, 2017
Oct 10-13, 2017
Feb 18-22, 2018
May 28-31, 2018
Aug 27-30, 2018
Sep 25-28, 2018
Dec 13-14, 2018
Apr 11 to May 09, 2019
b
H7
H8
H13
Normalized total CO2 flux

Figure 3

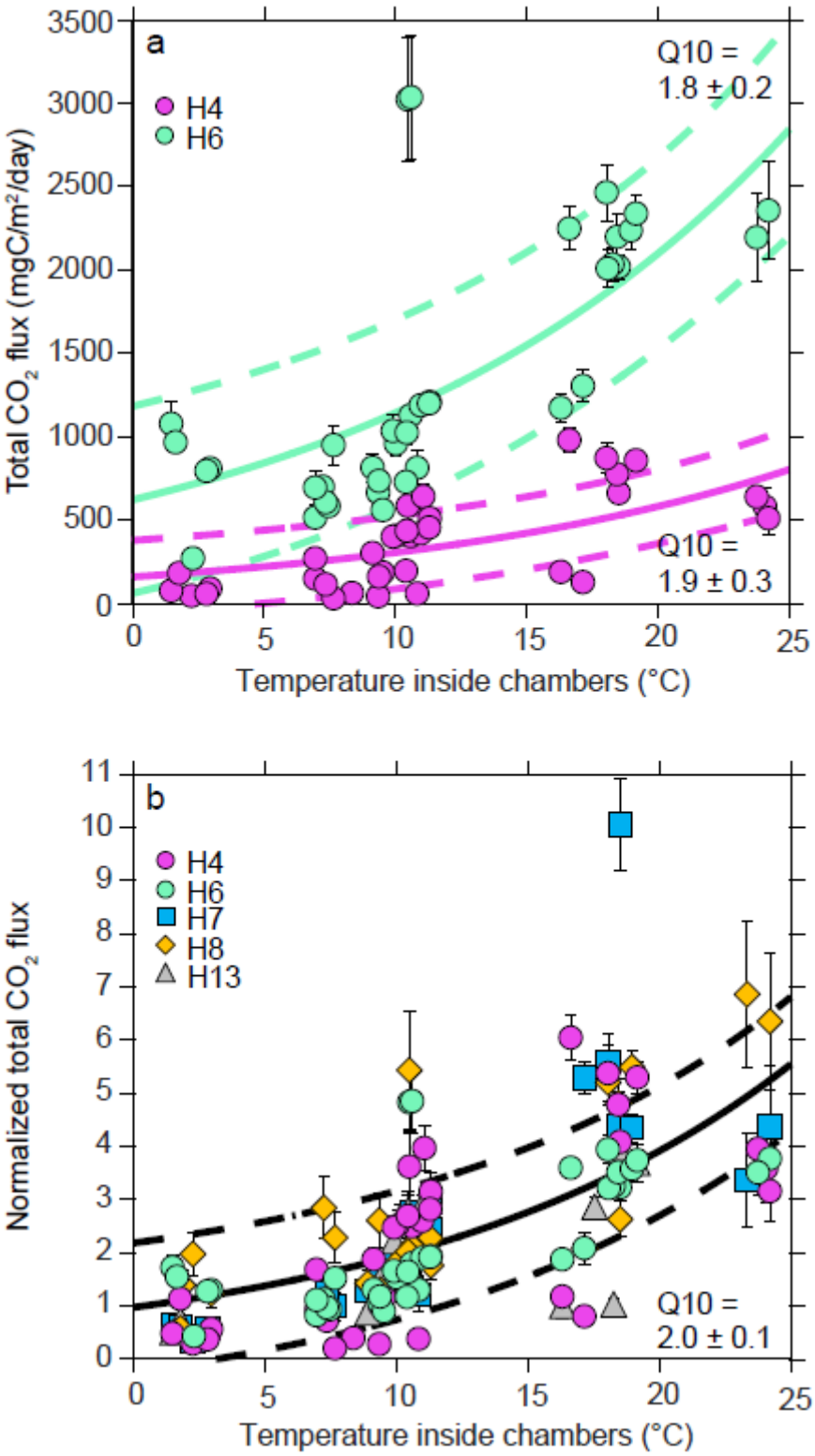
a
H4
H6
Q10 =
1.8 ± 0.2
Q10 =
1.9 ± 0.3
Total CO2 flux (mgC/m²/day)
Temperature inside chambers (°C)
b
H4
H6
H7
H8
H13
Q10 =
2.0 ± 0.1
Normalized total CO2 flux
Temperature inside chambers (°C)

Figure 4

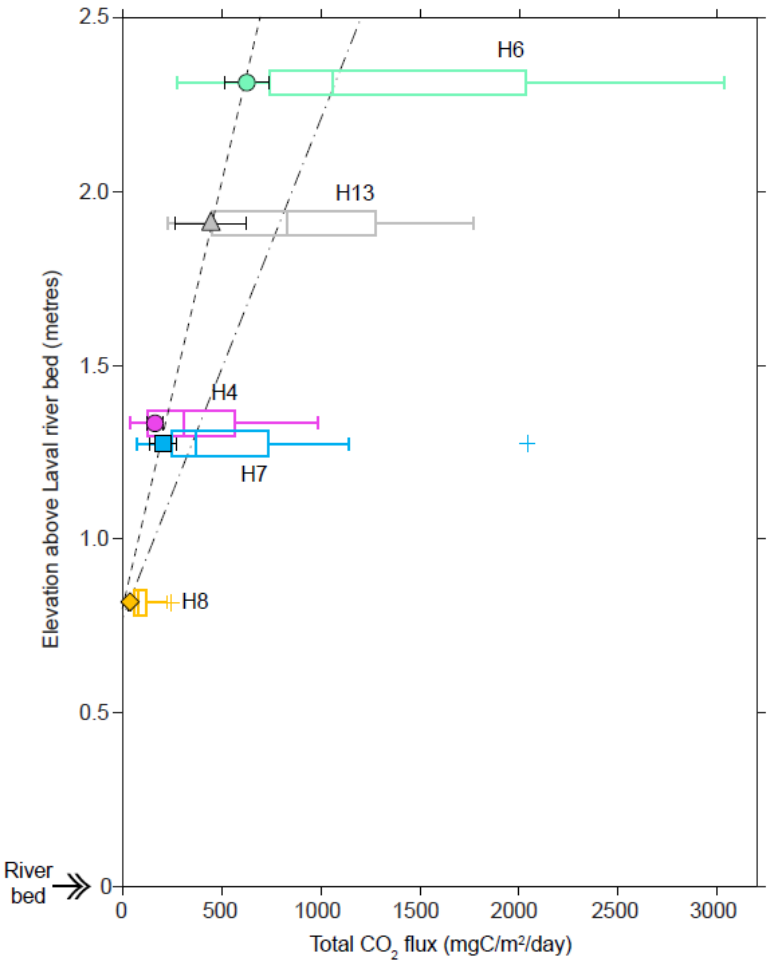
H6
H13
H4
H7
H8
Elevation above Laval river bed (metres)
2.5
2.0
1.5
1.0
0.5
0
River bed
0
500
1000
1500
2000
2500
3000
Total CO_2 flux (mgC/m²/day)

Figure 5

Extended Data

Extended Data Figures and Captions

Extended Data Figure 1: CO_2 emissions measured in the Laval catchment (Draix, France) (red square; Supplementary Table 4) compared to respiration CO_2 flux in various soil types (black hyphens). Median values are shown with the symbols, the minimum-maximum range is indicated with solid lines. As maximum value for cropland exceeds the scale of the y-axis, upper part of the cropland range is dashed and maximum value is indicated. The respiration soil compilation is from ref. [30]. Note that the CO_2 emission from oxidative weathering of sedimentary rocks in the Laval catchment reaches the magnitude of the CO_2 emissions from respiration of all type of soils.

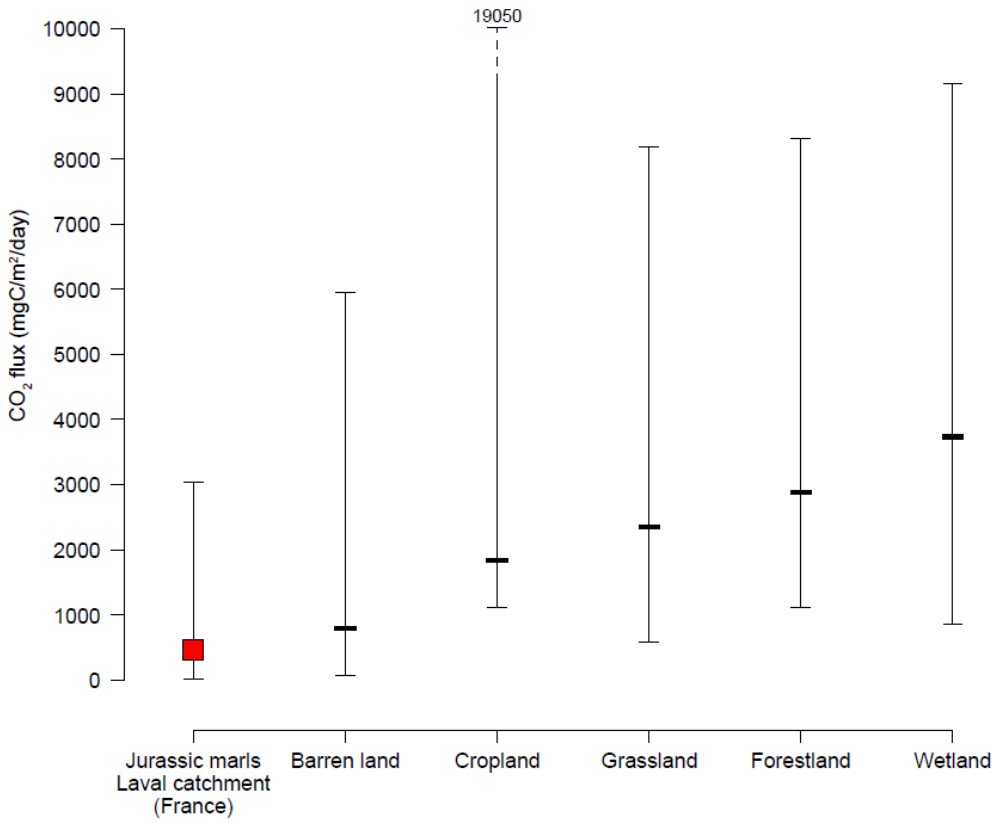

Extended Data Figure 2: Temperature and hydrological controls on total CO_2 emissions recorded in chambers H4 and H6 for one month from 10/04/2019 to 10/05/2019. Upper panel: Daily temperature average (black line) and amplitude (grey envelope) in the rock interior. Lower panels: CO_2 flux measured in chamber H4 (pink circles) and H6 (green circles). Error bars indicate standard deviation on the flux measurements (Methods) when larger than the symbol size. Circles with a black dot inside denotes CO_2 flux measurements performed in average 17 hours (15 to 19 hours) after a rainfall event. The rain events are visible as sharp peaks in the water discharge recorded in the Laval catchment (blue envelope).

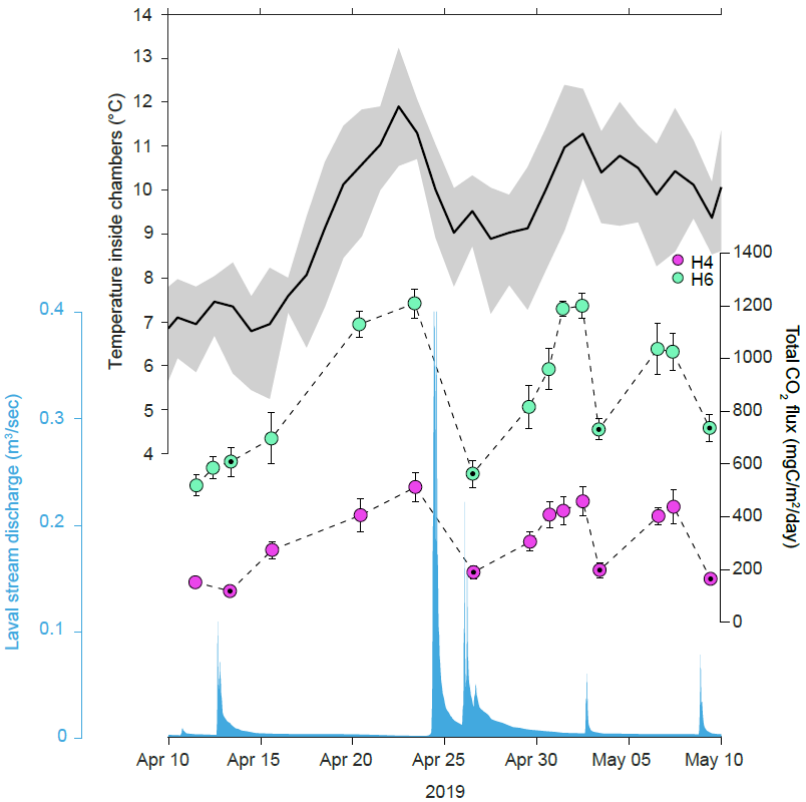

Extended Data Figure 3: Climate of the Laval catchment (Draix, France) for two and a half years from December 2016 to May 2019 (study period). Monthly rain precipitation (bars) is compared to the monthly temperature average (red line). Drought periods are represented by the orange bars. Rainfall monitoring in the Laval catchment started in 1982 (ref. 13,23). 2017 was the driest year ever recorded in the Laval catchment (annual precipitation 627 mm), whereas 2018 was the wettest (1327 mm), and 2019 the second wettest (1263 mm). Note the 4 month-long drought from July to October 2017. The climatic diagram shows the highly seasonal pattern of the air temperature in the Laval catchment.

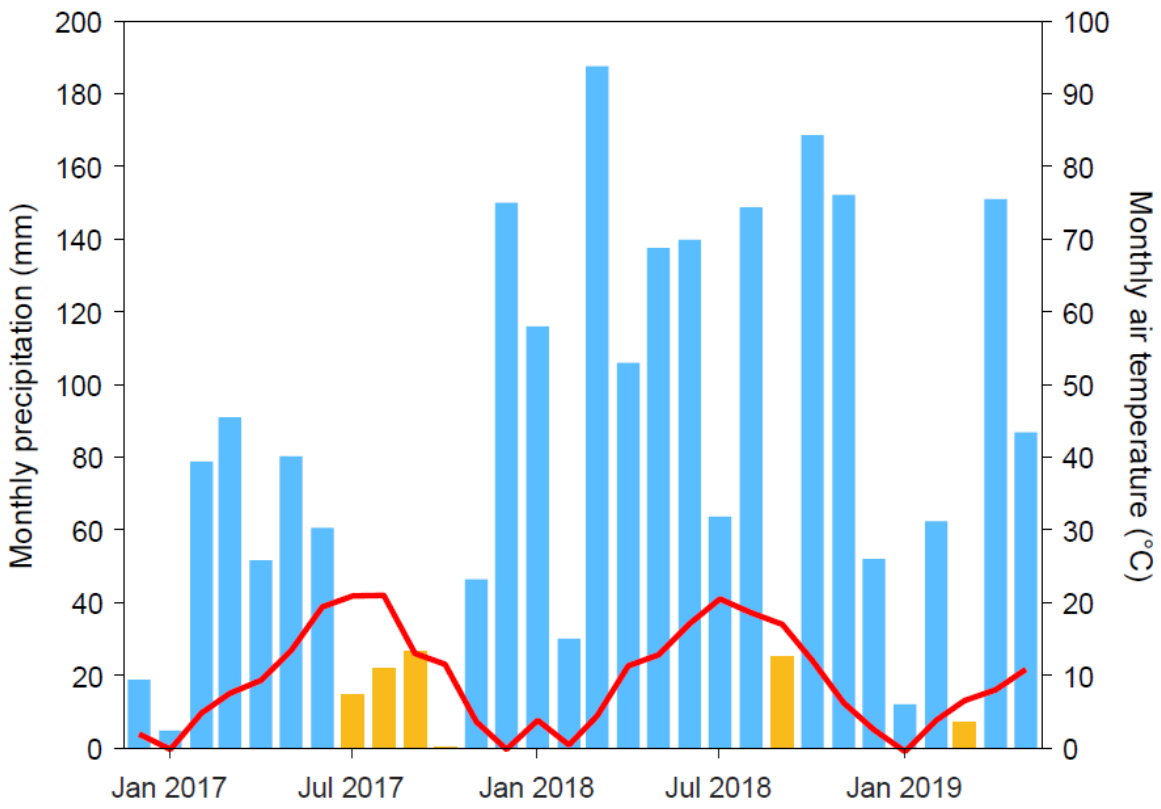

Extended Data Figure 4: a. The near surface water content of the Laval catchment marls at station B3 (red line) and B4 (blue line) and the daily-averaged air temperature (green line) at "Le Plateau" weather station (located ~500 metres from station B3 and B4) from 11/05/2016 to 29/11/2016 (ref. [36]). **b**. The near surface water content at station B3 (red circles) and B4 (blue circles) versus daily-averaged air temperature recorded at the "le Plateau" weather station. **c**. Box plots showing the variability of the near surface water content of the marls at station B3 (red) and B4 (blue) for the air temperature range -2 to 16°C and 16 to 24°C. Box plots show maximum, 25% percentile, median, 75% percentile and minimum values, as well as the mean (dot) and outliers (circles).

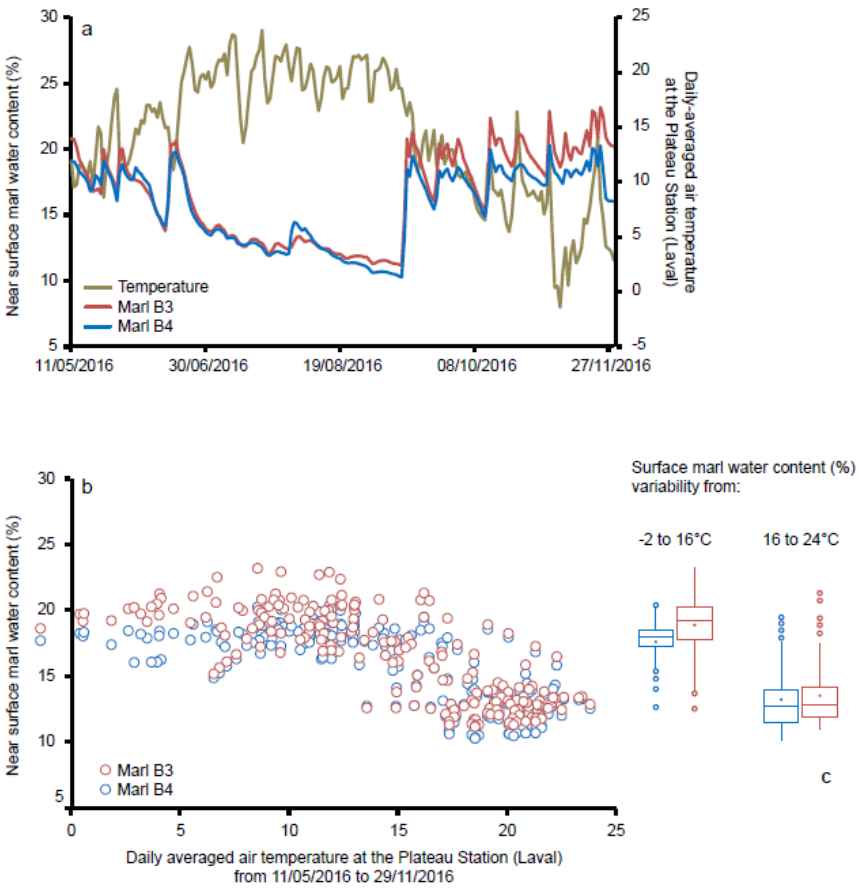

Extended Data Figure 5: Calibration between the daily averaged temperature measured in the rock chamber (y-axis) and the γ factor (x-axis). The calibration aims to reconstruct the temperature in the chamber (when we could not measure it) based on the air temperature (T_{air}) measured at the "Le Plateau" weather station (located 200 metres from the field site) and the fractional daylight duration (L) at the Laval catchment latitude. Note that the γ factor is a simple function of T_{air} and L: $\gamma = f(T_{air}, L)$. For further details see Methods (section Environmental data). Upper panel: circles are calibration data obtained over a 12-month period of overlap between measured chamber and air temperature. Blue line and its envelope are the best fit and the 95% confidence interval. Lower panel: Blue dots are the residuals between the chamber temperature and the fitted model. Red line is the zero line.

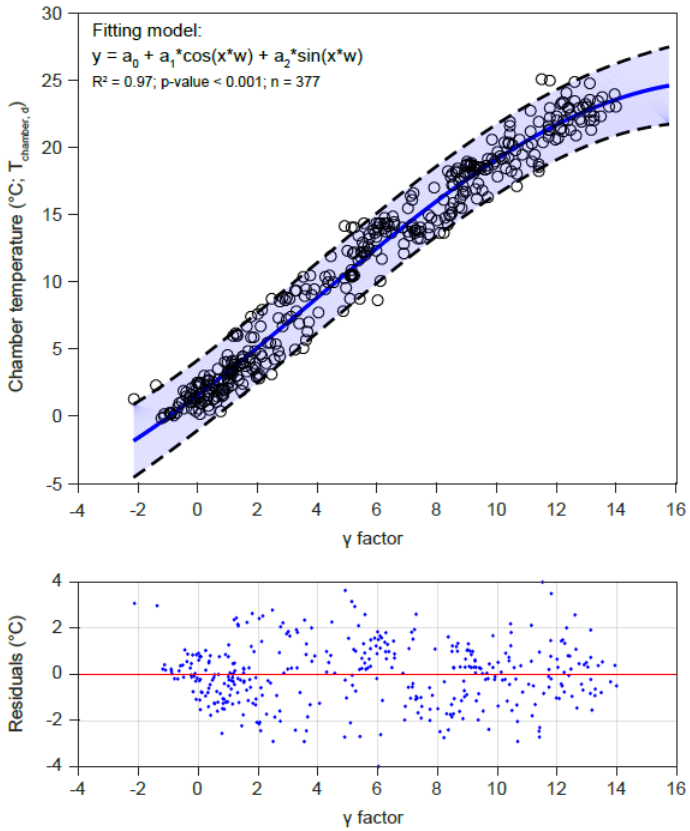

Extended Data Figure 6: Measured and reconstructed chamber temperatures. Blue line is the daily averaged temperature measured in the chamber. Light blue envelope is the daily amplitude between the minimal and maximal temperatures recorded daily. Dark grey line is the reconstructed temperature in the chamber (see Extended Data Figure 4 for the calibration). The light grey envelope is the 95% confidence interval. On the lower x-axis are shown the field work campaigns.

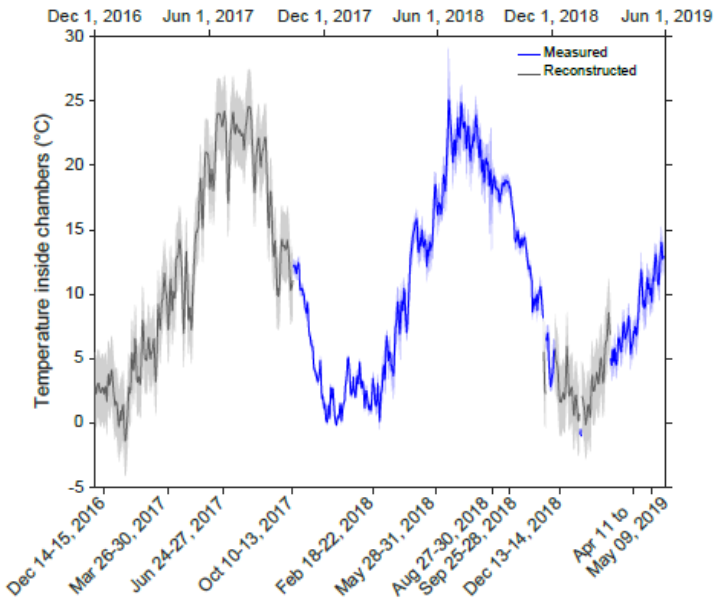
Dec 1, 2016
Jun 1, 2017
Dec 1, 2017
Jun 1, 2018
Dec 1, 2018
Jun 1, 2019
Measured
Reconstructed
Temperature inside chambers (°C)
30
25
20
15
10
5
0
-5
Dec 14-15, 2016
Mar 26-30, 2017
Jun 24-27, 2017
Oct 10-13, 2017
Feb 18-22, 2018
May 28-31, 2018
Aug 27-30, 2018
Sep 25-28, 2018
Dec 13-14, 2018
Apr 11 to
May 09, 2019